Journal of Fluids and Structures (2001) **15,** 1009–1030
doi:10.1006/jfls.2001.0383, available online at http://www.idealibrary.com on IDEAL®

NUMERICAL STUDIES OF TWO SIDE-BY-SIDE ELASTIC CYLINDERS IN A CROSS-FLOW

Y. Liu, R. M. C. So, Y. L. Lau and Y. Zhou

Department of Mechanical Engineering, The Hong Kong Polytechnic University Hung Hom, Kowloon, Hong Kong

(Received 12 January 2001, and in final form 25 April 2001)

Flow-induced vibrations of two side-by-side circular cylinders in a cross-flow at different spacing ratios and mass-damping parameters are examined numerically. The two cylinders are simply supported at both ends. Two different cases are considered: one is the rigid case where the structural stiffness of the cylinder is assumed to be infinite, and the other is the elastic case where the cylinders undergo oscillations. In the latter case, the cylinders vibrate under the action of the unsteady flow-induced forces. Both cases are simulated at a Reynolds number of 200, which represents a typical laminar flow. The present approach solves the unsteady flow field using a finite element method with a deforming grid to accommodate the moving cylinders. As for the cylinder motions, a two-degree-of-freedom structural dynamics model is invoked. Fluid–structure interactions are resolved through iteration at the same time step. Numerical calculations of the rigid case are validated against previously published results. Good agreement is obtained between the present calculations and the data. The calculated visualization is compared with its experimental counterpart and the flow patterns are found to be consistent with experimental observation. Finally, the flow behind the vibrating cylinders is analysed with an objective to understand the effect of cylinder motions on the near wake. The calculated flow patterns at different spacing ratios are found to be consistent with previously documented experimental observations.

1. INTRODUCTION

One approach to tackle the problem of flow-induced vibrations of high-rise buildings in close proximity is to develop an understanding of the interactions between the near-wake flow and the motions of the buildings. Complications of the wake flow behind bluff bodies have been extensively investigated (Zdravkovich 1997). Maull & Young (1973) found that the shedding phenomenon was greatly affected by the complexity of the oncoming stream, e.g., a bluff body in shear flow would lead to vortex shedding occurring in spanwise cells. Shedding was further complicated in the presence of neighbouring bluff bodies (Maull 1971). In this situation, depending on whether the bluff bodies were arranged in tandem or inline, they were affected differently by the vortices shed from the neighbouring cylinders and the nonuniformity of the oncoming flow. If the bodies were elastic, the motions of the bodies and their resulting effects on the surrounding flow will add to the complexity of the problem. A further complication is the very high Reynolds numbers usually encountered in flow-induced vibration of high-rise buildings. However, the basic physics of this problem could be gleaned from investigating an idealized situation at a relatively low Reynolds number. Therefore, as a first attempt, the problem could be modelled by multiple structures in close proximity with each other freely vibrating in a cross-flow in the laminar regime.

0889–9746/01/071009 + 22 $35.00/0

This approximation is justified because the physics of flow-induced vibration is largely governed by the vortex shedding behaviour and less by the physics of the surrounding flow (So *et al.* 2001). Understanding of the physics could be gained through experimental and/or numerical simulation of the flow around relatively simple arrangements of bluff bodies. The case of two side-by-side cylinders vibrating as a result of fluid forcing is one of the most basic and revealing problems in the general subject of vortex-induced fluid–structure interaction.

Numerous experimental studies have been performed on the flow around two side-by-side cylinders set normal to the free stream (Spivack 1946; Bearman & Wadcock 1973; Williamson 1985; Bearman 1995; Sumner *et al.* 1997, 1999; Paidoussis 1998; Zhou *et al.* 2001). Spivack (1946) investigated the predominant frequencies in the flow field behind a pair of cylinders using a hot wire technique over a Reynolds number ($\mathrm{Re} = U_\infty D/\nu$) range of $1{\cdot}5 \times 10^4$–$9{\cdot}3 \times 10^4$, and discovered three distinct regimes of flow with different spacing ratios T/D. Here, U_∞ is the free-stream velocity, D is the cylinder diameter, ν is the fluid kinematic viscosity and T is the spacing between cylinder centres. Bearman & Wadcock (1973) suggested that the repulsive forces acting between two circular cylinders were originated from a rotation of the resultant force created by the presence of the neighbouring cylinder. They also found that the asymmetry was due to a near-wake phenomenon and not to the position of the boundary layer separation. On the other hand, Williamson (1985) found the existence of harmonic vortex-shedding modes behind a pair of cylinders, and observed that the shedding frequency on one side of the wake was a multiple of that on the other. Sumner *et al.* (1997, 1999) studied the fluid–structure interaction phenomenon in a water tunnel. They found that the reported bistable nature of the biased flow was not detected in the water tunnel experiments. Consequently, they questioned whether this was a coincidence or whether there was a deeper underlying reason.

Compared to experimental studies, there have been relatively few numerical investigations of the flow around two circular cylinders. Stansby (1981) used an essentially inviscid discrete-vortex method to investigate two side-by-side cylinders in a cross-flow and was able to reproduce most of the gross wake features observed experimentally. Chang & Song (1990) simulated the flow around two side-by-side circular cylinders at $\mathrm{Re} = 100$ for $T/D = 1{\cdot}7$ and $3{\cdot}0$. They used a blending technique, which was made up of a finite-element method for the vicinity of the circular cylinders and a finite-difference method for the rest of the flow field, to tackle the problem. Tezduyar *et al.* (1990) used a finite-element formulation with the streamline-upwind/Petrov–Galerkin (SUPG) method to investigate a similar problem with $T/D = 1{\cdot}5$ and $\mathrm{Re} = 100$. On the other hand, Slaouti & Stansby (1992) studied the flow around two side-by-side circular cylinders using the random-vortex method. Their calculations were carried out at $\mathrm{Re} = 200$ and several T/D ratios. Most of the numerical investigations considered rigid cylinders only, where the cylinders are assumed to have infinite structural stiffness. Consequently, the interactions between the fluid and the elastic structures were not investigated.

The objective of the present study is to examine the fluid–structure interaction problem given rise by two side-by-side cylinders placed in a cross-flow. The numerical approach is a finite-element formulation using a deforming mesh to accommodate the arbitrary motions of the two cylinders. The method is an extension of that developed for a single cylinder (So *et al.* 2001). Thus, the interactions between the wake flow and the cylinder responses can be correctly modelled. This numerical approach has been validated against a freely vibrating cylinder in a cross-flow (So *et al.* 2001). Therefore, the present study needs to further verify the numerical technique for multiple rigid cylinders in order to establish its credibility when applied to perform design analysis of multiple structures in a cross-flow. As a first attempt, the emphasis is placed on calculating the case with $\mathrm{Re} = 200$ where the flow is essentially

laminar (Slaouti & Stansby 1992). The flow patterns in the wake derived from the calculations are compared, at least qualitatively, with the experimental flow visualization results obtained by Zhou *et al.* (2001) for three different T/D ratios. These comparisons attempt to firmly establish the credibility of the present numerical method to tackle fluid–structure interaction problems involving multiple structures. Interactions between structures and fluid are then thoroughly studied by considering three mass-damping parameters and three different T/D together and their influence on cylinder vibrations and spectral characteristics. The mass-damping parameter is defined as $M_r\zeta_s$, where M_r is the ratio of the cylinder mass to the mass of the displaced fluid and ζ_s is the dimensionless structural damping coefficient. The ratios, $T/D = 1{\cdot}1$, $1{\cdot}8$ and $3{\cdot}0$, are chosen because the flow regimes thus resulted are representative of three different proximity effects observed in two side-by-side cylinders (Zdravkovich 1985).

2. NUMERICAL METHODS AND DATA ANALYSIS

In the calculation of fluid–structure interaction problems, it is necessary to resolve the flow field, the structural dynamics and, most important of all, the fluid–structure interactions. If this last behaviour is not resolved correctly, the calculated flow-induced forces and hence the structural dynamics will be in error. In the following, the solution of the flow is described first, then the structural dynamics model, the resolution of the fluid–structure interactions and their feedback to the flow and structural dynamics solutions, and finally a discussion of the data analysis technique used. These techniques have been discussed in detail in So *et al.* (2001). However, for the sake of completeness, a brief description of these components is also given here.

2.1. Flow Calculation

A schematic view of the problem is shown in Figure 1. Two side-by-side elastic cylinders with fixed support at both ends are placed in a cross-flow with a free-stream velocity of U_∞. The computational domain is a $25D \times 16D$ rectangular region, the upstream length is about

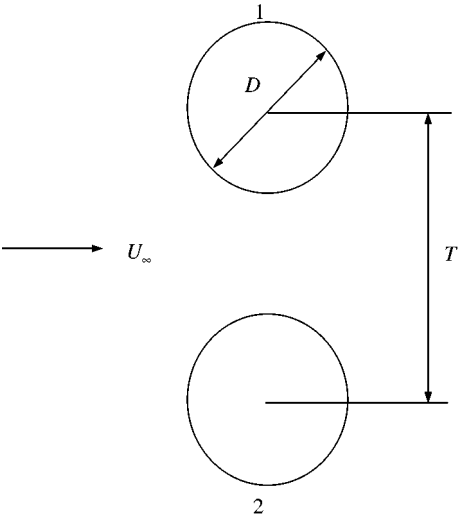

Figure 1. A schematic layout of two side-by-side cylinders in a cross-flow.

$5D$, while the downstream length is $20D$, and the two cylinders are symmetric about the centreline. The governing equations and their boundary conditions are given below for ease of reference:

$$\nabla \cdot \mathbf{u} = 0, \tag{1}$$

$$\frac{\partial \mathbf{u}}{\partial \tau} + \mathbf{u} \cdot \nabla \mathbf{u} = -\nabla p + \frac{1}{\mathrm{Re}} \nabla^2 \mathbf{u}. \tag{2}$$

In these equations, $\mathbf{x} = (x, y)$ is the Cartesian position vector, $\mathbf{u} = (u, v)$ is the velocity field, p is the pressure, τ is the time. All these variables are dimensionless and they are defined with respect to the dimensional variables (denoted here by the superscript *, except for time t) by $\mathbf{x} = \mathbf{x}^*/D$, $\mathbf{u} = \mathbf{u}^*/U_\infty$, $p = (p^* - p_\infty)/\rho U_\infty^2$ and $\tau = tU_\infty/D$. To complete the formulation, the boundary conditions have to be specified. They are

(i) at the upstream far field, domain top boundary and domain bottom boundary,

$$\mathbf{u} = 1, \tag{3}$$

(ii) at the downstream far field,

$$\frac{\partial \mathbf{u}}{\partial n} = 0, \tag{4}$$

(iii) at the surface of the cylinders,

$$\mathbf{u} \cdot \mathbf{n} = \mathbf{u}_{\mathrm{cy}} \cdot \mathbf{n}, \tag{5}$$

where n denotes the normal direction to the boundary, $\mathbf{u}_{\mathrm{cy}}$ is the velocity of the cylinders and $\mathbf{n}$ is the unit normal vector.

The Navier–Stokes equations are solved using a finite-element method (FEM) and the nonlinear coupling terms in the equations are treated separately, at different fractional time steps, by an operator-splitting time-stepping method. The method is suitable for both steady and transient problems and can readily be extended to include extra equations describing additional physical effects, such as the effects of cylinder motions on the flow field and *vice versa* (Bristeau *et al.* 1987).

The task in the present transient scheme is to find $\{\mathbf{u}^{m+1}, p^{m+1}\}$ at the $(m+1)$ time step from $\{\mathbf{u}^m, p^m\}$ at the mth time step. With the superscript m denoting the iteration number, the steps involved in generating the solution $\{\mathbf{u}^{m+1}, p^{m+1}\}$ are as follows:

(a) first fractional step

$$\frac{\mathbf{u}^{m+\delta} - \mathbf{u}^m}{\delta \Delta t} - \frac{\alpha}{\mathrm{Re}} \nabla^2 \mathbf{u}^{m+\delta} + \nabla p^{m+\delta} = \frac{\beta}{\mathrm{Re}} \nabla^2 \mathbf{u}^m - (\mathbf{u}^m \cdot \nabla)\, \mathbf{u}^m, \tag{6}$$

$$\nabla \cdot \mathbf{u}^{m+\delta} = 0, \tag{7}$$

(b) second fractional step

$$\frac{\mathbf{u}^{m+1-\delta} - \mathbf{u}^{m+\delta}}{(1-2\delta)\Delta t} - \frac{\beta}{\mathrm{Re}} \nabla^2 \mathbf{u}^{m+1-\delta} + (\mathbf{u}^{m+1-\delta} \cdot \nabla)\, \mathbf{u}^{m+1-\delta} = \frac{\alpha}{\mathrm{Re}} \nabla^2 \mathbf{u}^{m+\delta} - \nabla p^{m+\delta}, \tag{8}$$

(c) third fractional step

$$\frac{\mathbf{u}^{m+1} - \mathbf{u}^{m+1-\delta}}{\delta \Delta t} - \frac{\alpha}{\mathrm{Re}} \nabla^2 \mathbf{u}^{m+1} + \nabla p^{m+1} = \frac{\beta}{\mathrm{Re}} \nabla^2 \mathbf{u}^{m+1-\delta} - (\mathbf{u}^{m+1-\delta} \cdot \nabla)\, \mathbf{u}^{m+1-\delta}, \tag{9}$$

$$\nabla \cdot \mathbf{u}^{m+1} = 0. \tag{10}$$

In the above scheme, α, $\beta \in (0, 1)$ and $\alpha + \beta = 1$, $\delta \in (0, \frac{1}{3})$.

The subproblems at the first and third fractional steps are identical and are of the steady Stokes problem type, namely,

$$\alpha_0 \mathbf{u} - \frac{v_1}{\mathrm{Re}} \nabla^2 \mathbf{u} + \delta \nabla p = \mathbf{F}_1, \tag{11}$$

$$\nabla \cdot \mathbf{u} = 0, \tag{12}$$

where $\mathbf{F}_1$ is a body force, $\alpha_0 = 1/\Delta t$ and $v_1 = \alpha\delta$. On the other hand, the subproblem at the second fractional step is of the type of a classical nonlinear diffusion–convection problem, namely,

$$\alpha_0 \mathbf{u} - \frac{v_2}{\mathrm{Re}} \nabla^2 \mathbf{u} + (1 - 2\delta)(\mathbf{u} \cdot \nabla)\mathbf{u} = \mathbf{F}_2, \tag{13}$$

where $\mathbf{F}_2$ is also a body force and $v_2 = \beta(1 - 2\delta)$. A good choice for δ (Bristeau *et al.* 1987) was found to be $(1 - 1/\sqrt{2})$. The value of α and β are chosen in such a way that $v_1 = v_2$ is satisfied to yield identical Helmholtz operators at all fractional steps, which contribute considerably to the overall efficiency of the operator-splitting algorithm.

The steady quasi-Stokes problem (11) is solved by a preconditioned conjugate gradient method. The nonlinear diffusion–convection problem (13) is reformulated as a least square problem and solved by a preconditioned conjugate gradient method. This scheme reduces the solution of the Navier–Stokes equations to solve a sequence of scalar Dirichlet problems associated with the Helmholtz operator and the Neumann problems associated with the Laplacian operator. The matrix associated with the Helmholtz operator is well conditioned for all Re, since $\alpha_0 = 1/\Delta t$.

The variational form of the above numerical system is discretized by the Galerkin finite-element method. Quadratic triangular elements are used throughout. Six-node quadrilateral elements are used for velocity and three-node linear elements are used for pressure. Integration by parts is implemented for all the diffusion terms.

The program development was carried out in a high level language *Fasttalk*, which is a unique feature of *Fastflo*, a general-purpose finite-element CFD package developed by CSIRO (Stokes 1994). *Fastflo* contains neither physical assumptions nor mathematical algorithms; it purely supports *Fasttalk* language, assemblies and solves the finite-element equations programmed by *Fasttalk*. A comparison between calculations and measurements of an elastic cylinder in a cross-flow up to $\mathrm{Re} \approx 5000$ has been carried out and good agreement was obtained (So *et al.* 2001).

Since the boundary layer is expected to be thin near the cylinder, a fine mesh is concentrated near the cylinder surface. The number of panels is 256, the number of nodes is about 63 589, and the number of elements is numerically determined to be about 31 589, which is adequate to resolve the velocity and the boundary layers. These numbers are determined by using different meshes, from coarse to progressively finer meshes, until the drag coefficient is mesh-convergent to within a prescribed tolerance of about 0·5%.

2.2. Cylinder Dynamics

The circular cylinders are assumed to be modelled by a spring–damper–mass system, which is representative of the location of maximum amplitude of vibration at the mid-section of a long cylindrical structure mounted with fixed ends. Thus, the cylinder motions can be

accounted for by solving a two-degree-of-freedom dynamic equation for each cylinder,

$$\ddot{\mathbf{Z}} + \frac{4\pi\zeta_s}{U_r}\dot{\mathbf{Z}} + \left(\frac{2\pi}{U_r}\right)^2 \mathbf{Z} = \frac{\mathbf{C}_f}{2M_r}, \tag{14}$$

where $\mathbf{Z} = (X/D)\mathbf{i} + (Y/D)\mathbf{j}$, X and Y denote the instantaneous displacements of the cylinders in the x and y directions, respectively, $M_r = M/(\rho D^2)$ is the mass ratio, ρ is the air density and M is the cylinder mass per unit length. The force coefficient is defined as $\mathbf{C}_f = 2\mathbf{F}/\rho U_\infty^2 D$, while the reduced velocity is given by $U_r = U_\infty/f_n^* D$, where f_n^* is the natural frequency of the stationary cylinder. The two-dimensional force vector, $\mathbf{F} = \{F_D, F_L\}$, consists of the unsteady drag and lift force components. Their corresponding coefficient is defined as $C_D = 2F_D/\rho U_\infty^2 D$ and $C_L = 2F_L/\rho U_\infty^2 D$, respectively. The solution yields the vibration displacement and the velocity of the cylinder as they respond to the surrounding flow field and the motion of the shed vortices. The incompressible flow calculation is coupled with the cylinder responses through the boundary conditions and $\mathbf{C}_f$, thus allowing fluid–structure interactions to be adequately resolved at each time step if the flow calculation and equation (14) are solved iteratively. In the present formulation, this iteration is carried out at each time step until the induced forces and the cylinder motions give rise to convergent results.

2.3. Fluid–Structure Coupling

The major difficulty associated with the numerical simulation of viscous flow around the oscillating cylinders is to describe boundary conditions at the moving boundary within a finite-element grid system. In the present problem, the two side-by-side elastic cylinders are free to vibrate within the flow domain, and the reference frame cannot be attached to the cylinder. Therefore, a deforming computational mesh is required to accommodate the arbitrary motion of the two cylinders. The cylinder surfaces are adjusted according to the motion of the cylinders by means of nodal displacement. At each time step the displacements of the cylinders are calculated, represented by the vector function $\mathbf{Z}(X/D, Y/D)$. In order to distribute the mesh deformation as uniformly as possible, i.e., to minimize local mesh deformation and prevent potential entanglements, a Laplacian equation of displacement is solved throughout the computational domain with the cylinder displacements as the boundary condition. The Laplacian equation and boundary condition can be written as

$$\nabla^2 \boldsymbol{\delta} = \mathbf{0} \tag{15}$$

with $\boldsymbol{\delta} = \mathbf{0}$ at the outside boundary and $\boldsymbol{\delta}_i = \mathbf{Z}_i$ at each cylinder wall. The entire computational mesh is adjusted by a Laplacian interpolation, which is designed to map a mesh smoothly onto a reasonably similar shape, specified by the displacements of the elastic cylinders. As a result, the mesh nodal coordinates have changed, but the connectivity of the mesh remains constant, and the flow field solution is projected from the old mesh onto the new one.

During the calculation, the reference frame is fixed in the far field. Therefore, the cylinders are free to vibrate within the calculation domain. At each time step, the fluid flow is solved using the finite-element method. The force on each cylinder is calculated by integrating the pressure and the wall shear stress on the surface. This is then taken as the force input for equation (14) and the response of each cylinder is calculated by solving equation (14) using the Runge–Kutta method. Each cylinder is moved according to the displacement, and the mesh is remapped according to this motion. Then the flow field is solved again using the cylinder velocity as the boundary condition. Finally, the whole process is repeated in an

iterative way so that the interactions between the fluid and the cylinders are accounted for properly.

2.4. Data Analysis

The calculated and measured time series are analysed using the auto-regressive moving average (ARMA) technique. Details of the ARMA technique can be found in Mignolet & Red-Horse (1994). The use of this technique to analyse time series derived from flow-induced vibration problems has been attempted (Jadic *et al.* 1998; Zhou *et al.* 1999; So *et al.* 2001) before and the results have been compared with those obtained from the Fast Fourier transform method. The technique was found to be quite suitable for flow-induced vibration problems (Jadic *et al.* 1998).

3. COMPARISON WITH PUBLISHED DATA FOR TWO RIGID CYLINDERS

The validity of the proposed numerical method for multiple structures is examined by making a thorough comparison between the present calculations and previously reported numerical data and experimental flow visualization results. The numerical results of Slaouti & Stansby (1992) are selected for the comparison together with the visualization experiments of Zhou *et al.* (2001). These two comparisons are reported separately below.

3.1. Comparison with Previously Reported Numerical Data

The calculations attempted are two rigid cylinders placed in a cross-flow with $\mathrm{Re} = 200$ and $T/D = 1{\cdot}1$, $1{\cdot}8$ and $3{\cdot}0$. These three cases have also been reported earlier by Slaouti & Stansby (1992). Furthermore, the flow visualization experiments of Zhou *et al.* (2001) were carried out at $\mathrm{Re} = 150$ and $T/D = 1{\cdot}13$, $1{\cdot}7$ and $3{\cdot}0$. Thus, the calculations of these three cases can be compared with the two sets of reported data. The present calculations and the published results are tabulated in Table 1. From this point on, the subscripts 1 and 2 are used to denote cylinder 1 and 2, respectively, as indicated in Figure 1. In order to deduce the root mean square values from the reported results, the amplitudes of the fluctuating forces are divided by $\sqrt{2}$.

TABLE 1
Comparison of the present calculations with other two cylinder results at $\mathrm{Re} = 200$

	$T/D = 1{\cdot}1$		$T/D = 1{\cdot}8$		$T/D = 3{\cdot}0$	
	Present calculation	Slaouti & Stansby (1992)	Present calculation	Slaouti & Stansby (1992)	Present calculation	Slaouti & Stansby (1992)
$\bar{C}_{D1}$	1·806	1·85	1·185	1·10	1·03	1·23
$\bar{C}_{D2}$	1·806	1·85	1·123	1·30	1·12	1·22
C'_{D1}	0·2295	0·212	0·066	0·25	0·066	0·11
C'_{D2}	0·2292	0·283	0·086	0·25	0·086	0·07
$\bar{C}_{L1}$	1·172	0·89	0·328	0·35	0·116	0·14
$\bar{C}_{L2}$	− 1·173	− 0·90	− 0·299	− 0·13	− 0·120	0·00
C'_{L1}	0·566	0·424	0·103	0·50	0·133	0·71
C'_{L2}	0·567	0·389	0·091	0·57	0·133	0·64
f_{s1}	0·1101	0·11	$f_{s1}^{(1)}$ 0·162	0·16	0·19	0·215
			$f_{s1}^{(2)}$ 0·223	0·26		
f_{s2}	0·1101	0·11	$f_{s2}^{(1)}$ 0·162	0·16	0·19	0·215
			$f_{s2}^{(2)}$ 0·223	0·26		

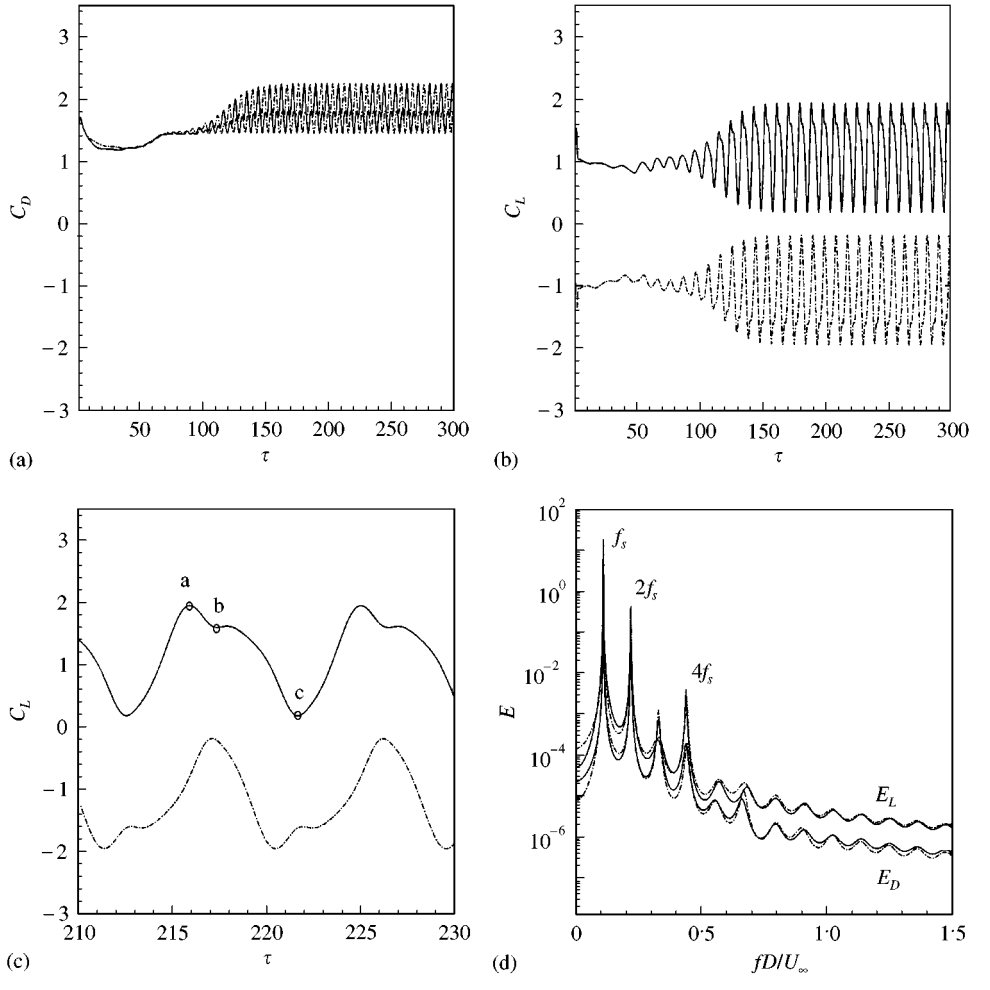

Figure 2. Two rigid cylinders at $T/D = 1{\cdot}1$ and Re = 200; (a) C_D time series; (b) C_L time series; (c) enlarged view of C_L for a short period of time, where "point a" indicating the time at the lift peak of cylinder 1, "point b" being the time at the turning point before the additional peak, and "point c" being the time at the lift valley of cylinder 1; and (d) power spectra of C_L and C_D. ——, Cylinder 1; –·–·–, Cylinder 2.

At $T/D = 1{\cdot}1$, the calculated mean drag coefficient, $\bar{C}_D$, for both cylinders is the same. This trend is identical with that given by Slaouti & Stansby (1992) and the difference between the $\bar{C}_D$ results is only 2.4%. The values of the mean lift coefficient, $\bar{C}_L$, of the two cylinders are equal but antithetical. This trend, too, bears a striking resemblance to that obtained by Slaouti & Stansby (1992), thus indicating a repelling force between the two cylinders. The difference in $\bar{C}_L$ between the present calculations and those of Slaouti & Stansby (1992) is about 23%. As shown in Figure 2(a, b), the drag and lift forces oscillate in-phase and at the same frequency. This is evident from the calculated shedding frequencies for the two cylinders, which are $f_{s1} = f_{s2} = 0{\cdot}11$ for the present calculations as well as for those reported by Slaouti & Stansby (1992). The power spectra of C_L and C_D for both cylinders are shown in Figure 3(d). Here, E is the ARMA power spectral density, which is defined as the square norm of the system function scaled by the sampling interval and

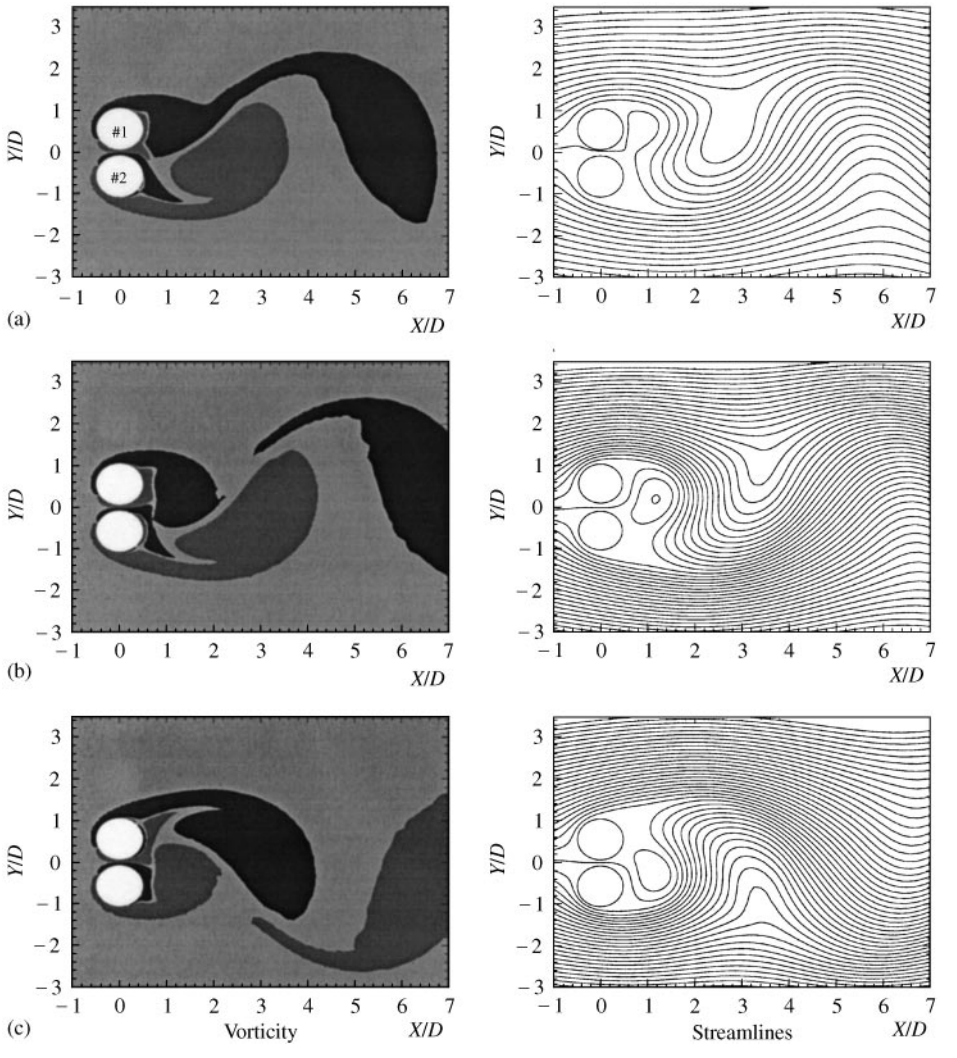

Figure 3. Vortex formation and streamline patterns for two rigid cylinders at $T/D = 1{\cdot}1$.

white-noise variance (Marple 1987). At this Re and T/D, both cylinders have the same shedding frequencies and harmonics. The present calculations give the same root mean square fluctuating drag coefficient, C_D', for the two cylinders. The same is also true for the root-mean-square fluctuating lift coefficient, C_L'. On the contrary, there is a difference between the two cylinders in the calculated C_D' and C_L' in the results reported by Slaouti and Stansby (1992). Generally speaking, at this T/D, it is clear that the present calculations and the results reported earlier (Slaouti & Stansby 1992) are similar and fairly consistent.

In Figure 2(a, b), the lift and drag time series are approximately periodic. However, at each period, besides the positive peak, there exists a small additional peak, as shown in the enlarged view in Figure 2(c). This additional peak is not the noise in the signal, rather, it is the interaction of the gap flow with the vortex shedding. In order to observe the development of the vortex formation, three "time points" are marked in Figure 2(c). These points are denoted as a, b and c, where "point a" indicates the time at the lift peak of cylinder 1,

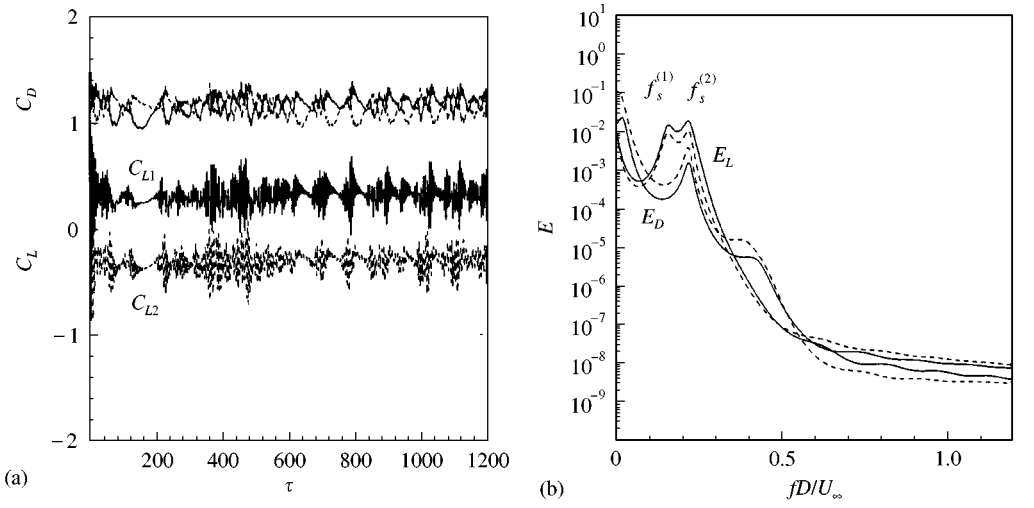

Figure 4. Two rigid cylinders at $T/D = 1{\cdot}8$ and Re = 200; (a) C_L and C_D time series, and (b) power spectra of C_L and C_D. ——, Cylinder 1; – – –, Cylinder 2.

"point b" is the time at the turning point before the additional peak and "point c" is the time at the lift valley of cylinder 1. The vortex formation and streamlines for $T/D = 1{\cdot}1$ at the three "time points" marked in Figure 2(c) are shown in Figure 3. It can be seen that the gap flow is very weak and deflects periodically around the bases of the upper and lower cylinders. This is consistent with the downstream vortex shedding shown in Figure 3(a, c), which are half a period apart. At "point a", a larger vortex has shed from cylinder 2 (lower), a smaller vortex is developing from the outer shear layer of cylinder 1 (upper), and the deflection of the gap flow is toward cylinder 1, i.e., the cylinder where the vortex shedding is taking place. Even though the gap flow is very weak, the inner boundary layers are still developing between the two cylinders. This can be inferred from the vorticity distribution plot shown in Figure 3(a) where a small vortex exists behind cylinder 2. At "point b", the lift time series of cylinder 1 is at its turning point, i.e., just before the additional peak. The previous smaller vortex developed from the outer shear layer of cylinder 1 is growing and trying to merge with the small vortex developed from the gap flow. The additional peak is caused by this merging of the bigger vortex from the outer shear layer of cylinder 1 and the small vortex developed from the gap flow. At "point c", the vortex developed from the outer shear layer of cylinder 1 has shed, a new vortex is developing from the outer shear layer of cylinder 2, the gap flow changes its direction from upward to downward, and the lift time series is at its valley.

An inspection of Figure 4(a) shows a strong irregularity in the time series of lift and drag at $T/D = 1{\cdot}8$. The calculation time is quite long ($\tau = 1200$), but it seems that a stationary state has not been reached. Therefore, it is possible that there is no stationary state for this case. The irregularity might not be due to transition behaviour, but due to vortex interactions. The power spectra of C_L and C_D for both cylinders at $T/D = 1{\cdot}8$ are shown in Figure 4(b). There are two dominant peaks for C_L, reflecting the two vortex shedding frequencies. The two shedding frequencies are identified as the first and second shedding frequencies, denoted here by $f_s^{(1)}$ and $f_s^{(2)}$, respectively. The present calculation gives $f_s^{(1)} = 0{\cdot}162$, essentially the same as that reported by Slaouti & Stansby (1992); but the difference in $f_s^{(2)}$ between the two calculations is approximately 14%. The difference in $\bar{C}_D$ between the two calculations is less than 13%, but the C_D' given by Slaouti & Stansby (1992) is much

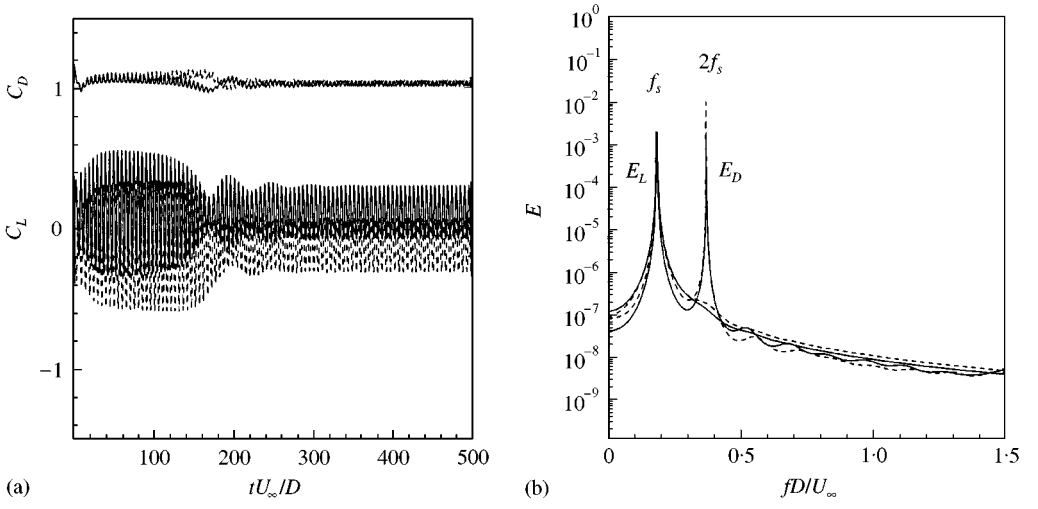

Figure 5. Two rigid cylinders at $T/D = 3{\cdot}0$ and Re = 200; (a) C_L and C_D time series, and (b) power spectra of C_L and C_D. ——, Cylinder 1; – – –, Cylinder 2.

higher than that of the present calculation. The values of the mean lift coefficient, $\bar{C}_L$, of the two cylinders are antithetical, indicating a repelling force between the two cylinders. This trend, too, bears a striking resemblance to that obtained by Slaouti & Stansby (1992). It should be pointed out that the magnitude of $\bar{C}_L$ for cylinders 1 and 2 is essentially the same for the $T/D = 3{\cdot}0$ and 1·1 cases. However, there is a substantial difference between the magnitude of $\bar{C}_L$ for cylinders 1 and 2 for $T/D = 1{\cdot}8$. The essentially equal repelling force calculated for the cases $T/D = 3{\cdot}0$ and 1·1 follows from the rather symmetric flow behaviour in the wakes of the two cylinders and the relatively stationary nature of the wakes. On the other hand, the unequal repelling force calculated in the $T/D = 1{\cdot}8$ case could be attributed to the biased flow pattern in the gap, which leads to a bistable behaviour of the gap flow, and the fact that the wake flow is not stationary even at $\tau = 1200$. This difference in behaviour of the gap flow is even more evident when a comparison of the present calculations of the wake flow is made with visualization results in Section 3.2.

At $T/D = 3{\cdot}0$, the lift and drag time series are again quite periodic, but they require a much longer time than expected to reach true stationary state, as shown in Figure 5(a). In the time period $\tau = 20$–160, the C_L signal appears to be almost stationary. However, after that period, the amplitude of C_L starts to decrease drastically and then increases eventually to reach the true stationary state after $\tau = 300$. The calculated mean drag coefficient, $\bar{C}_D$, for both cylinders is the same (Table 1). This trend is identical with that given by Slaouti & Stansby (1992), but their C'_D is much higher than the present calculation. The calculated $\bar{C}_L$ of the two cylinders are almost equal but antithetical, indicating a repelling force between the two cylinders. In the reported result (Slaouti & Stansby 1992), the mean lift of cylinder 2 is zero, and C'_L of both cylinders are much higher than those of the present calculation. The most likely explanation for this discrepancy is that their calculation time was not long enough, since they did not report the amplitude change between $\tau = 160$–200 and only showed the C_L and C_D time series in the period $\tau = 0$–120. An inspection of Figure 5(b) shows identical shedding frequencies for both cylinders (see also Table 1), thus indicating two identical vortex streets from the cylinders. The shedding frequency of C_D is also exactly double that of C_L. In spite of these similarities, the present calculated shedding frequency is less than that reported.

From this comparison, it is evident that the present numerical formulation is capable of reproducing the three different flow regimes that characterized the near wake of two side-by-side cylinders in a uniform stream corresponding to three different T/D ratios. The present calculations are also in fair agreement with the results reported earlier (Slaouti & Stansby 1992). However, the present calculations reveal that the flow takes a much longer time to reach stationary state. This could be the reason for the observed discrepancy between the present statistical results and those of Slaouti & Stansby (1992). The resolution is fine enough to reveal the second vortex shedding in the case $T/D = 1{\cdot}1$. This too was not reported previously.

3.2. Comparison of Wake Flow with Experimental Visualization

Having compared the statistics of the present numerical simulation of two side-by-side rigid cylinders in a uniform cross-flow with the results of Slaouti & Stansby (1992), the next comparison is made with the flow visualization results of Zhou *et al.* (2001). The visualization experiments were carried out for a number of T/D ratios and several Re. The closest Re available for comparison is 150 with $T/D = 1{\cdot}13$, $1{\cdot}7$ and $3{\cdot}0$, compared to the present calculations of $\mathrm{Re} = 200$ and $T/D = 1{\cdot}1$, $1{\cdot}8$ and $3{\cdot}0$. This comparison is viable because the wake flow is laminar at both Re. The experiments were carried out in a small water tunnel with acrylic cylinders of 6 mm diameter and the blockage was about 13.3% for all three T/D ratios. The cylinders were not exactly rigid; however, the displacements were so small that their effects on the wake flow were insignificant. Details of the experiment were given in Zhou *et al.* (2001); therefore, they will not be repeated here. It should be pointed out that flow visualization investigations were carried out over the domain $0 \leq x/D \leq 10$. Therefore, the calculations shown in the following comparison are also limited to this x/D range. Since the exposure time is different from the time step used in the simulation, the calculations over approximately the same time period are averaged before comparing.

The vortex comparison between numerical simulation and experimental visualization is shown in Figure 6. Generally, the calculated flow pattern looks similar to the experimental visualization. At $T/D = 1{\cdot}13$, the calculated vortex looks very much like the experimental visualization, and the two cylinders behave in a similar fashion to a single bluff body, i.e., a single vortex street is observed in the combined wake of the two cylinders. At intermediate T/D ($1{\cdot}7$ for the experiment and $1{\cdot}8$ for the calculation), the biased flow patterns are found in both numerical simulation and experimental visualization. In this comparison, the flow deflects downward and the biased flow of the numerical simulation is much more visible than that of the experimental visualization. In the actual case, the biased flow for both numerical and experimental studies is found to be bistable. At $T/D = 3{\cdot}0$, the flow field regains its symmetry, and the side-by-side rigid cylinders behave more as independent, isolated bluff bodies. In the current numerical simulation, the in-phase vortex shedding is the predominant fluid behaviour. In the experimental visualization, both in-phase and anti-phase vortex formations were observed, although the anti-phase was noted for the most part of the experimental visualization. The pictures in Figure 6 show the in-phase vortex shedding for both the numerical simulation and experimental visualization at $T/D = 3{\cdot}0$. Generally, the calculated flow pattern is quite consistent with the experimental visualization, indicating a correct simulation of the flow field behind the two side-by-side rigid cylinders.

4. RESULTS ON TWO ELASTIC CYLINDERS

Having verified the suitability of the numerical approach for multiple rigid cylinders in a cross-flow, the next step is to use it to study the case of two side-by-side elastic cylinders.

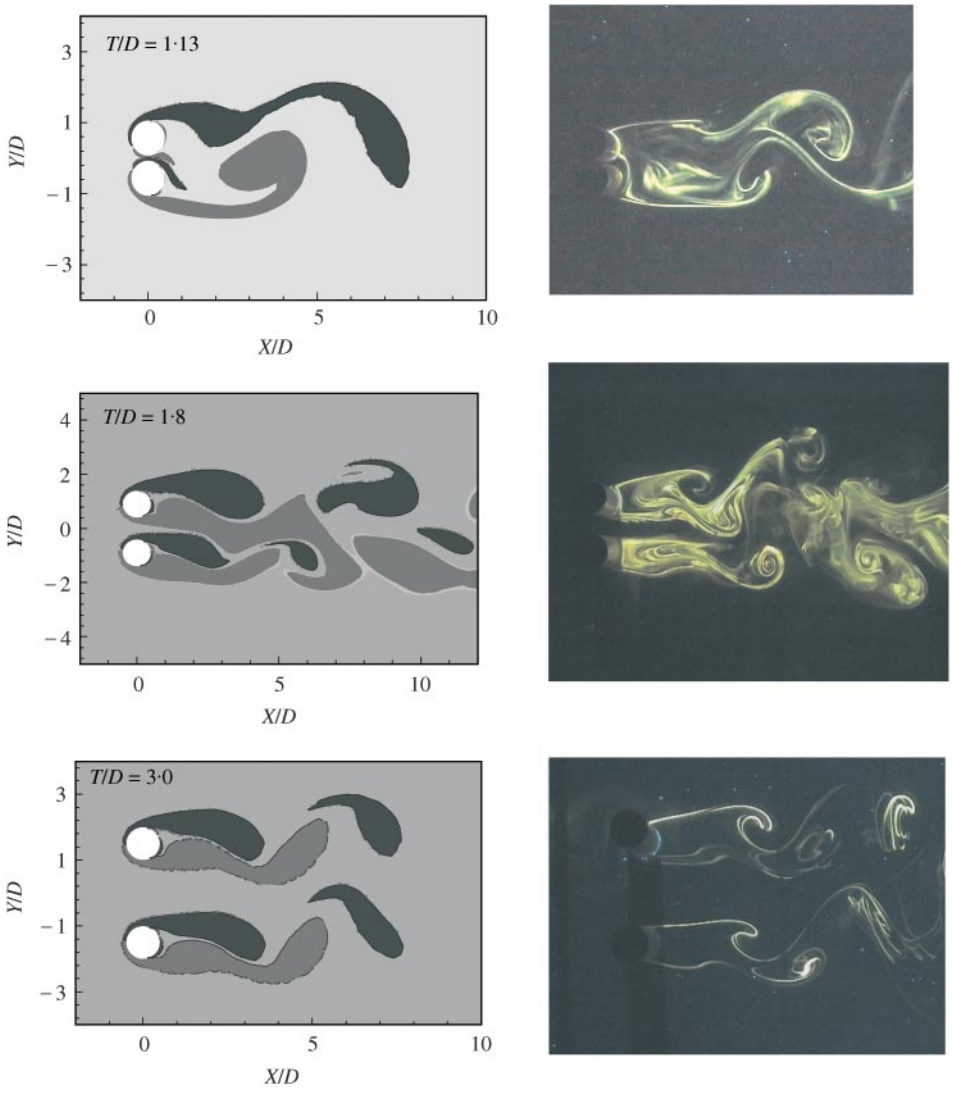

Figure 6. Visualization comparisons with experiment: (top) calculation and experiment at $T/D = 1{\cdot}13$; (middle) calculation at $T/D = 1{\cdot}8$ and experiment at $T/D = 1{\cdot}7$; (c) calculation and experiment at $T/D = 3{\cdot}0$.

In the present numerical simulation, the two cylinders are free to vibrate in the flow domain. A moving mesh is implemented to accommodate the arbitrary motion of the two cylinders. However, the two cylinders are not permitted to touch each other, and this limits the selection of $M_r\zeta_s$. In the present calculations, $M_r\zeta_s$ is selected to be 0·3, 1·0 and 2·0, and the corresponding mass ratios are $M_r = 10$, 33 and 66, respectively. For all calculations, $\mathrm{Re} = 200$ and $U_r = 5{\cdot}0$ are specified and the T/D ratios are chosen to be identical to those for the rigid case discussed above. This choice of parameters is to allow the effects of flow-induced vibration on the response of the elastic cylinders to be assessed. Therefore, in the following, whenever necessary, the results of the rigid case are also shown for comparison.

At this stage, experimental measurements are not available for comparison. The experiments of Zhou *et al.* (2001) were carried out at a much higher Re. It is the intent of the

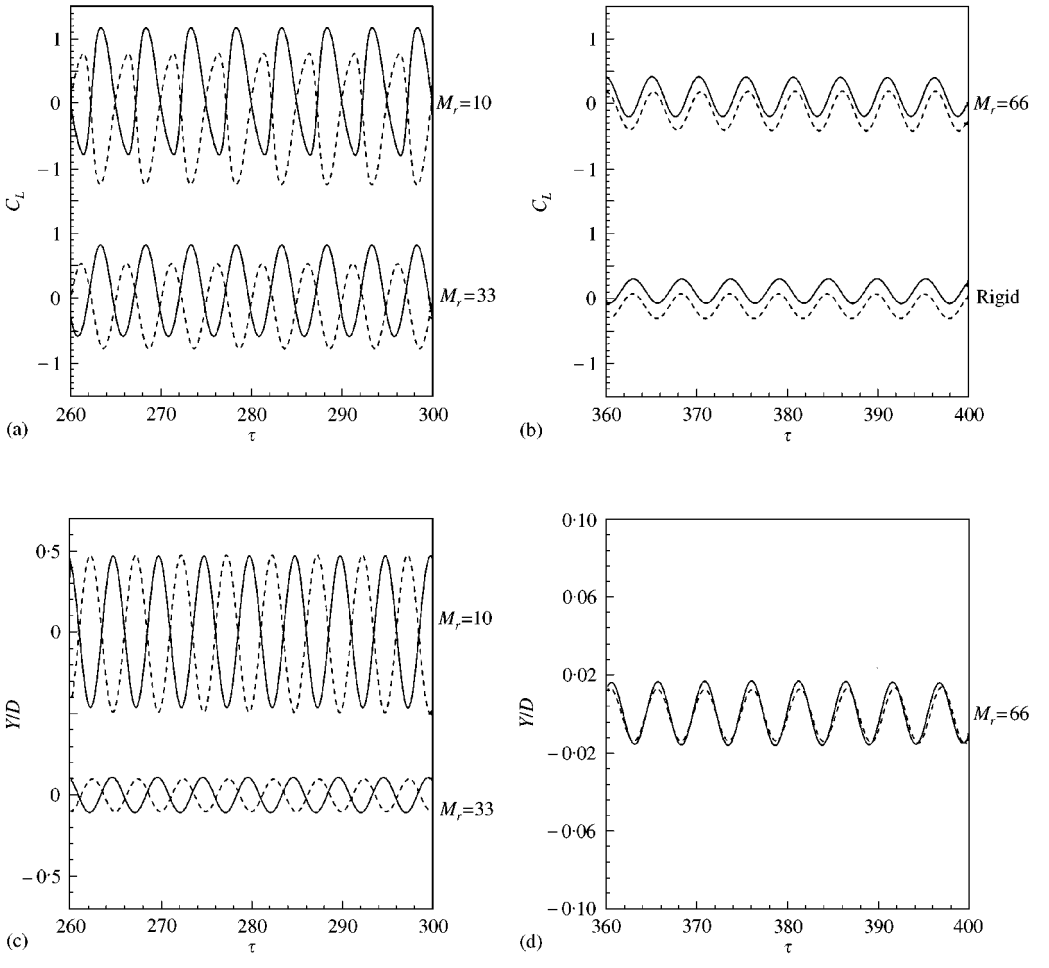

Figure 7. The C_L and Y/D time series for different M_r at $T/D = 3{\cdot}0$; (a) C_L comparison for $M_r = 10$ and 33, (b) C_L comparison for $M_r = 66$ and the rigid case, (c) Y/D comparison for $M_r = 10$ and 33, and (d) Y/D comparison for $m^* = 66$. ——, Cylinder 1; – – –, Cylinder 2.

present study to first establish firmly the credibility of the calculation method before extending it to higher Re. Therefore, the comparison with the experiments of Zhou *et al.* (2001) will be the subject of another paper. In the following, the discussion on $T/D = 3{\cdot}0$ is given first, this is followed by the case of $T/D = 1{\cdot}8$ and ends with the case of $T/D = 1{\cdot}1$.

4.1. Spacing Ratio of $T/D = 3{\cdot}0$

The C_L and transverse displacement (Y/D) time series of the two cylinders at $T/D = 3{\cdot}0$ with different M_r are shown in Figure 7. Generally, the amplitude of C_L and Y/D increases with decreasing M_r (or $M_r\zeta_s$). When the two cylinders are rigid, the oscillations of C_L for both cylinders are in-phase, indicating an in-phase vortex shedding. The level of C_L for cylinder 2 is lower than that of cylinder 1 and is consistent with the mean lift coefficients shown in Table 1. As the cylinders become elastic and $M_r = 66$, the amplitude of C_L is apparently larger than that of the rigid case, but the vibrations of the two cylinders are still in-phase. The level of C_L is still lower for cylinder 2. When the mass ratio is further reduced to

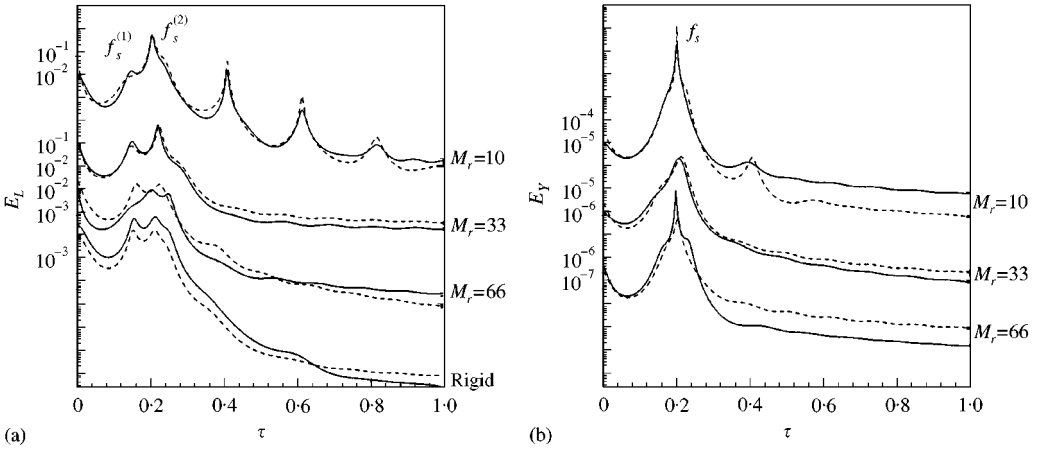

Figure 8. The power spectral density of C_L and Y/D at $T/D = 3{\cdot}0$ with different M_r; (a) C_L, (b) Y/D. ——, Cylinder 1; – – –, Cylinder 2.

$M_r = 33$ and 10, the vibrations of the two cylinders become anti-phase, and the amplitudes of C_L and Y/D become much larger. At $M_r = 10$, the peak-to-peak value of Y/D is approximately 1 and is quite large. In other words, the deforming computational mesh proves to be viable even for this relatively large deformation. The effect of flow-induced vibration on the cylinder dynamics is clearly visible; the nature of the cylinder vibration has been changed from that of in-phase to that of anti-phase, and the cylinders have been able to extract more energy from the flowing fluid to increase the vibration amplitudes.

The power spectra of C_L with different M_r are shown in Figure 8(a). For rigid and elastic cylinders, the vortex shedding frequency f_s is nearly identical. In the rigid case, there is only one peak in the spectral density of C_L, indicating a linear vortex shedding. When the cylinders are elastic, due to the strong interaction between fluid and structure, higher harmonics appear, indicating a nonlinear vortex shedding, and the nonlinearity increases with decreasing M_r. On the other hand, the power spectra of Y/D show an identical vibration frequency for all M_r calculated [Figure 8(b)]. This is indicative of the occurrence of resonance at $U_r = 5{\cdot}0$. Comparing Figure 8(a, b), it is apparent that resonance occurs with f_s of the rigid/elastic cylinder equaling f_n, the natural frequency of the fluid–cylinder system of the individual cylinder. At this $T/D = 3{\cdot}0$, the cylinder behaves as if the neighbouring cylinder has no influence. As a result, f_s of the two cylinders are identical and so is f_n of the fluid–cylinder system of the individual cylinder.

Vortex formation and streamline patterns behind the two cylinders for the $T/D = 3{\cdot}0$ case are shown in Figure 9. Here, the designation "attractive" indicates the case where the two cylinders with $M_r = 10$ are at their maximum attractive displacements, and "repulsive" denotes the case where the two cylinders with $M_r = 10$ are at their maximum repulsive displacements. In the rigid case, vortex shedding is in-phase. This leads to the formation of a single, binary vortex street in the combined wake of the two cylinders. The calculated phenomenon bears a striking resemblance to the case reported by Williamson (1985). When the two cylinders are elastic and $M_r = 10$, the two cylinders vibrate vigorously and vortex shedding is anti-phase. This behaviour is observed irrespective of whether the cylinders are "attractive" or "repulsive". The behaviour gives rise to two parallel vortex streets in the wake and the patterns for the two cases are quite similar. Again, this phenomenon is consistent with that reported by Williamson (1985). Therefore, further evidence in support of the present numerical technique is obtained.

4.2. Spacing Ratio of $T/D = 1{\cdot}8$

At this T/D, a biased flow pattern for the two cylinders is found. This biased flow is bistable. The cylinder towards which the flow is biased has a narrower near-wake and a higher f_s, while the other cylinder has a wider near-wake and a lower f_s.

The vortex formation and streamlines of the two cylinders at $T/D = 1{\cdot}8$ are shown in Figure 10, where Figure 10(a) displays the rigid case, and Figure 10(b, c) those of the elastic cases at $M_r = 10$. According to Williamson (1985), for $\mathrm{Re} \leq 200$, there are two types of basic behaviour in the vortex dynamics of the combined wake for the biased flow pattern. In the first case, vortices formed alongside the biased gap flow are squeezed and amalgamated into

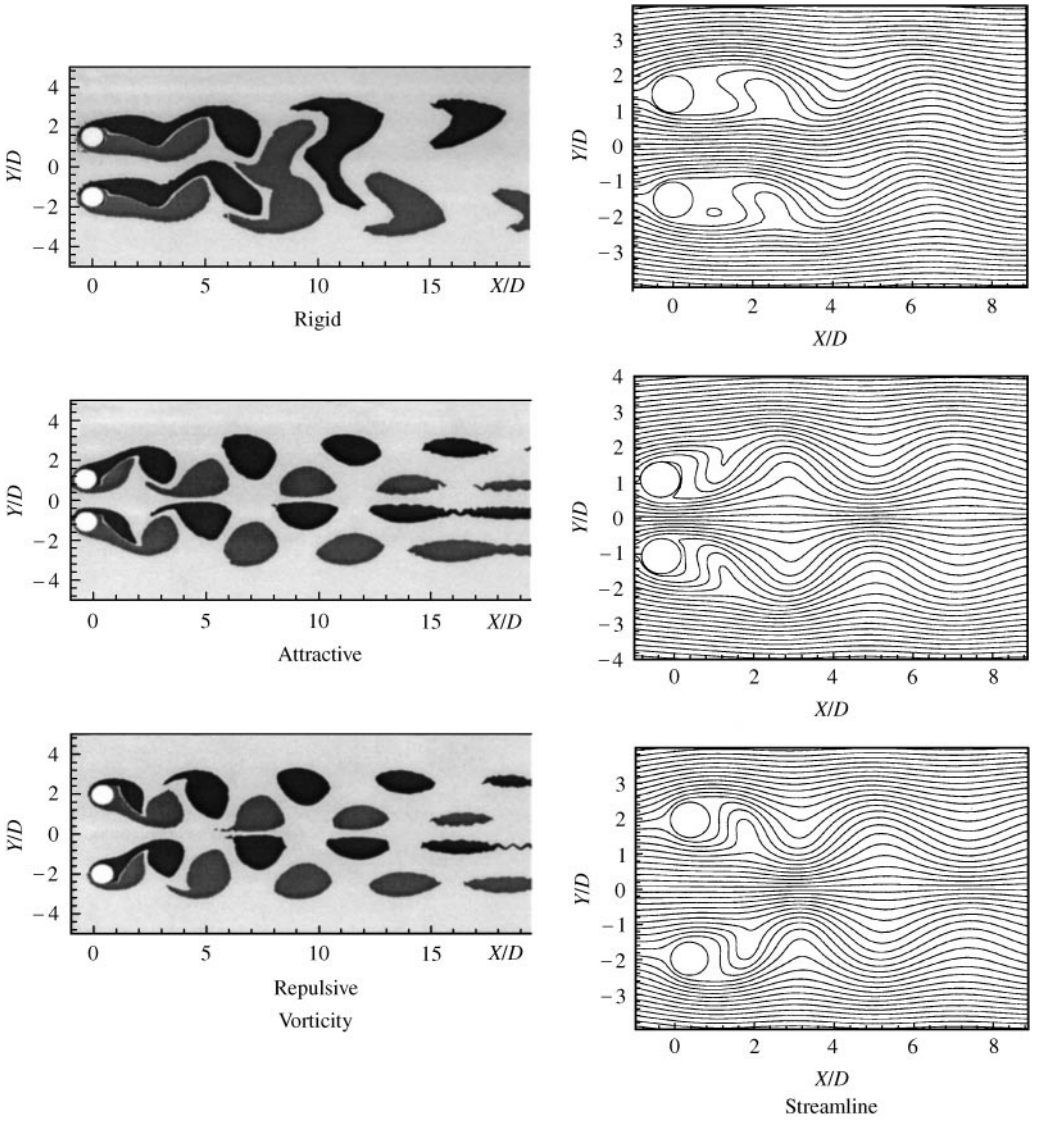

Figure 9. Vortex formation and streamline patterns for two cylinders at $T/D = 3{\cdot}0$.

the dominant vortices on the outside of the two-cylinder configuration, the side to which the flow is biased. This amalgamation process eventually produces a single vortex street in the combined wake. In the present calculation, Figure 10(a, b) exactly show the simulation of this phenomenon. In the second case of Williamson (1985), the combined wake of the two cylinders is marked by pairs of vortices downstream of the cylinder with the narrow near-wake region, and single larger vortices downstream of the cylinder with the wider near-wake region, on the opposite side. In this case, the gap vortices are amalgamated into the side of the wake where the pairs form. Again, the present result bears a striking resemblance to this phenomenon, as shown in Figure 10(c). Actually, in the present simulation, the two types of basic behaviour dominate alternatively the vortex formation for the case of $T/D = 1{\cdot}8$.

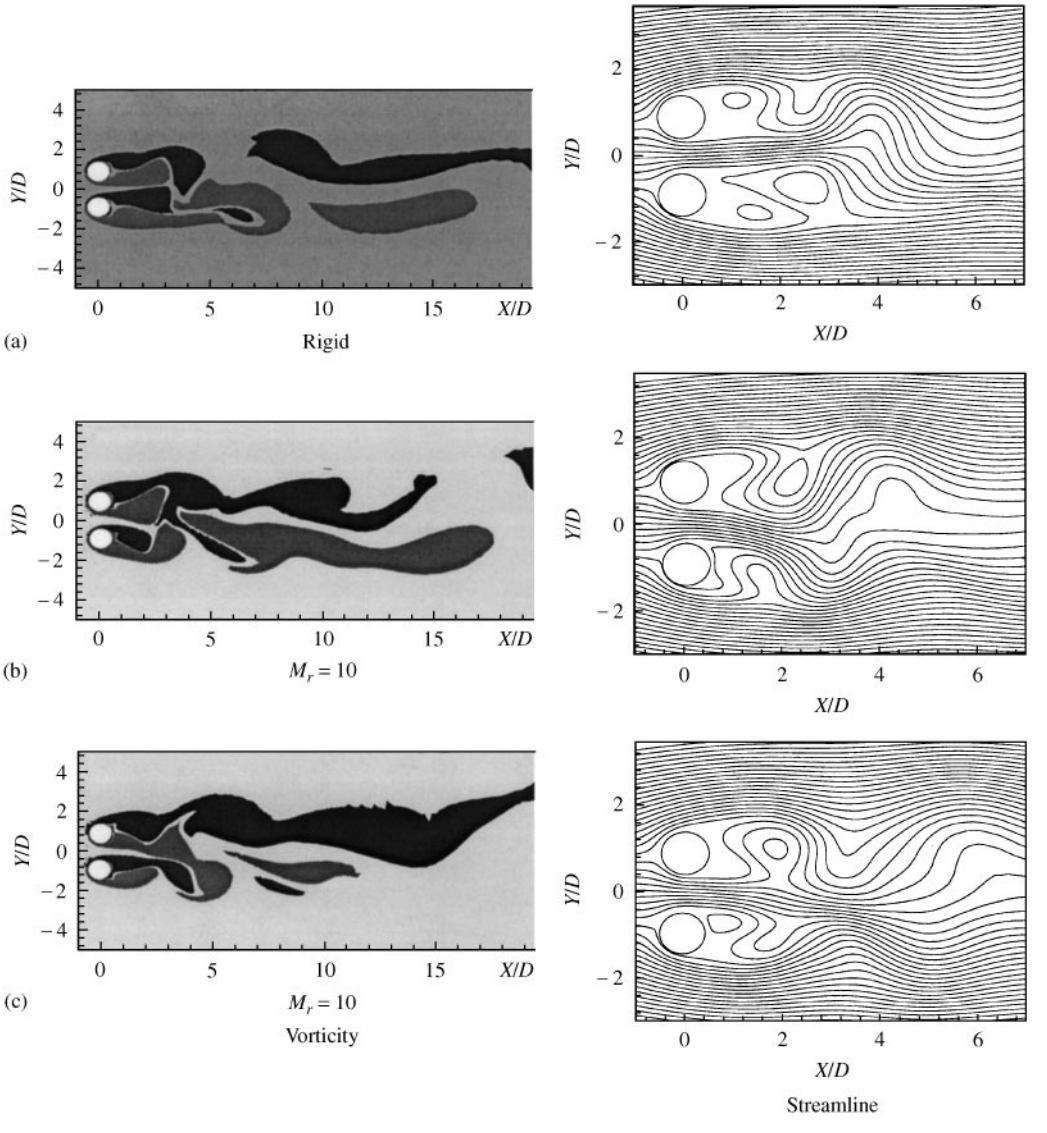

Figure 10. Vortex formation and streamline patterns for two cylinders at $T/D = 1{\cdot}8$.

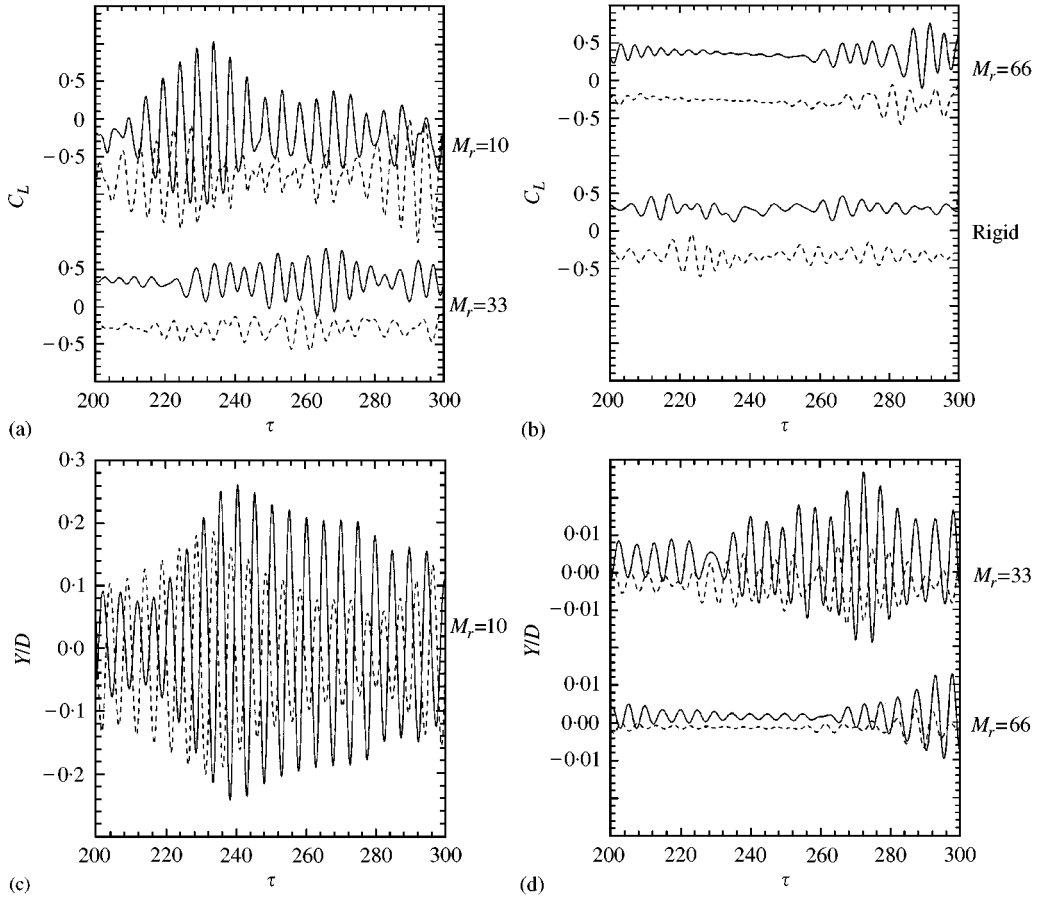

Figure 11. The C_L and Y/D time series for different M_r at $T/D = 1{\cdot}8$: (a) C_L comparison for $M_r = 10$ and 33; (b) C_L comparison for $M_r = 66$ and the rigid case; (c) Y/D comparison for $M_r = 10$; (d) Y/D comparison for $M_r = 33$ and 66. ——, Cylinder 1; – – –, Cylinder 2.

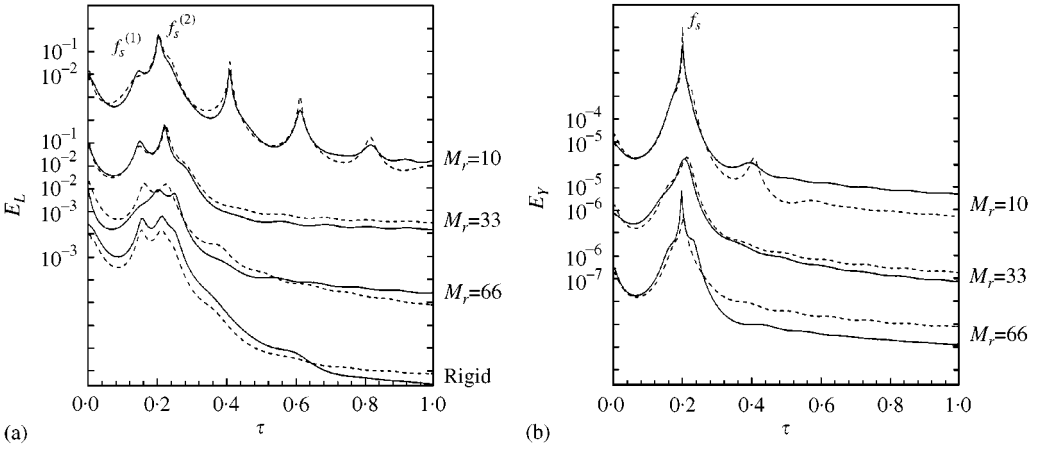

Figure 12. The power spectra of C_L and Y/D at $T/D = 1{\cdot}8$ with different M_r: (a) C_L; (b) Y/D. ——, Cylinder 1; – – –, Cylinder 2.

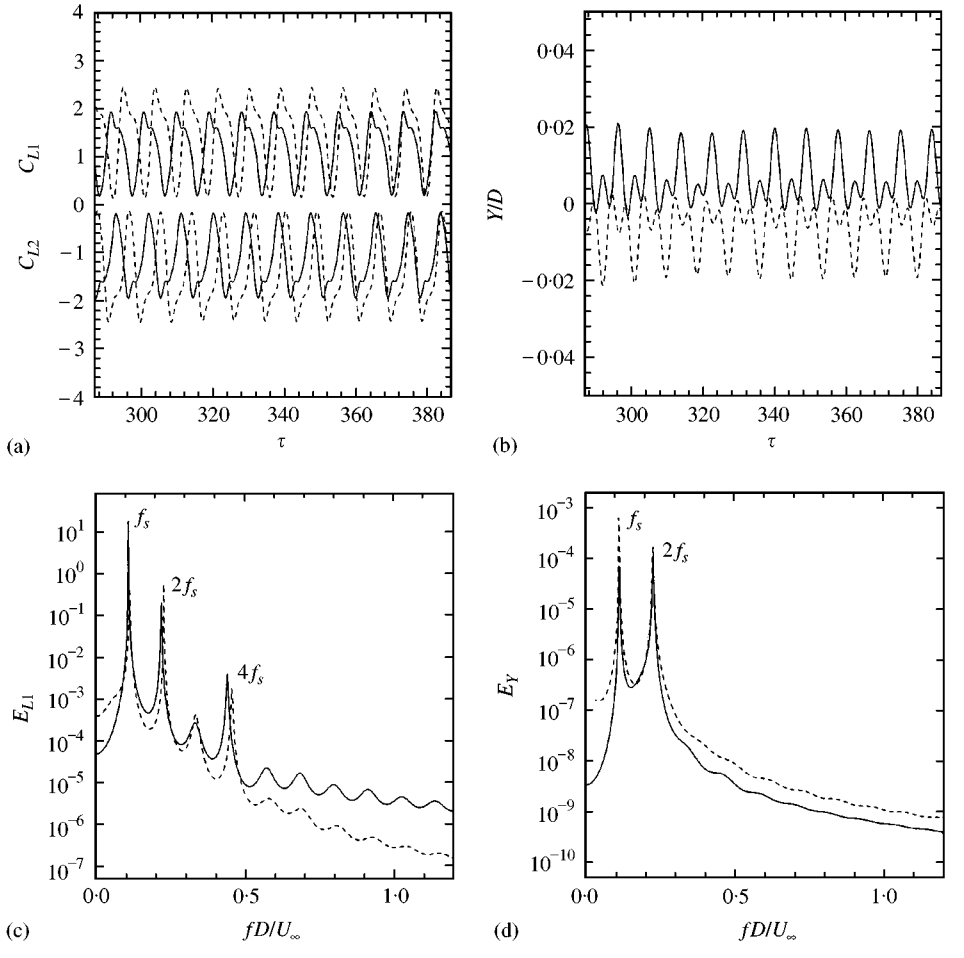

Figure 13. Two cylinders at $T/D = 1{\cdot}1$ and Re = 200; (a) C_L time series comparison between rigid and elastic ($M_r = 66$) cylinders, – – –, $M_r = 66$; ——, rigid. (b) Y/D time series for $M_r = 66$, (c) power spectra of C_L, and (d) power spectra of Y/D. ——, Cylinder 1; – – –, Cylinder 2.

The C_L and Y/D time series of the two cylinders at $T/D = 1{\cdot}8$ with different M_r are shown in Figure 11. Due to the strong interaction of the vortices in the near-wake and the irregular alternation of the types of vortex formation, the C_L and Y/D time series are also irregular and there is no observable stationary state in either time series, even for large time. An inspection of Figure 11(a, b) shows a strong dependence of the C_L amplitude on M_r, and its increase with decreasing M_r. Both in-phase and anti-phase vortex shedding exist in the time series for the rigid and the elastic cases, thus indicating a pattern of alternate vortex formation. The Y/D time series for different M_r are shown in Figure 11(c, d). Just as in the $T/D = 3{\cdot}0$ case, the Y/D amplitude of cylinder 1 is larger than that of cylinder 2 and it increases significantly with decreasing M_r.

The power spectra of C_L for the same T/D are shown in Figure 12(a) while those for Y/D are given in Figure 12(b). At this T/D, two dominant peaks are detected in E_L, reflecting two shedding frequencies, $f_s^{(1)}$ and $f_s^{(2)}$, just as in the rigid cylinder case discussed earlier. The values of $f_s^{(1)}$ and $f_s^{(2)}$ determined for cylinder 2 are very close to those given in Table 1 for the rigid case. There is a shift for cylinder 1 in the $M_r = 66$ case, but no shift for other M_r.

This shifting is also observed in experimental measurement for two rigid cylinders. As a result, the measured shedding frequencies are scattered, and Sumner *et al.* (1999) suggest that the scatter of the data simply shows that there is some variation in the magnitude of the two frequencies at a given T/D. For the rigid case and the elastic case where $M_r = 66$, no higher harmonics in the power spectra are detected, indicating linear vortex shedding. As M_r decreases to 10, higher harmonics are present and they are very strong, indicating nonlinear vortex shedding. On the other hand, the power spectra of Y/D show that there is only one dominant f_s [Figure 12(b)], except for $M_r = 10$ where a second peak is also noticed. This second peak occurs at a frequency that is $\sim 2f_s$ and could be due to cross talk between the lift and drag direction.

4.3. Spacing Ratio of $T/D = 1{\cdot}1$

At this T/D, the two cylinders are very close. The requirement that the cylinders should not touch each other limits the investigation to large M_r. Consequently, only the case of $M_r = 66$ is selected for investigation. When the cylinders are elastic, the amplitude of C_L increases slightly for both cylinders, as shown in Figure 13(a). An additional peak appears in the C_L time series. This is due to the interaction of the gap flow with the near wake, as shown in Figure 3 for the rigid case. At $U_r = 5{\cdot}0$, this additional peak has a strong influence on the vibration of the cylinders, as shown in Figure 13(b). Due to the strong interaction between the vortices developed from the outer shear layers of the cylinders and the gap flow, higher harmonics in the C_L power spectra of cylinder 1 are very prominent [Figure 13(c)], indicating nonlinear vortex shedding at $T/D = 1{\cdot}1$. Compared to the rigid case, the vortex shedding frequency of the elastic cylinders shifts slightly, as shown in Figure 13(a, c). The power spectra of Y/D show that two frequencies dominate the vibration of the cylinders, one is f_s while the other is $\sim 2f_s$. Again, this shows a strong cross talk between the lift and the drag direction.

5. CONCLUSIONS

A numerical study of the flow-induced vibration of two side-by-side cylinders in a cross-flow has been carried out at $\mathrm{Re} = 200$. An operator-splitting time-stepping finite-element method is used to solve for the flow field, while a two degree-of-freedom structural dynamics model is assumed for the cylinder motion. The cylinders do not move in the rigid case; however, they vibrate freely in the elastic case. Therefore, a deforming computational mesh is used to accommodate the arbitrary motion of the two cylinders. Each cylinder is allowed to move according to its displacement and the mesh is remapped as a result. After each such remapping, the flow field is solved again using the cylinder velocity as the boundary condition. The present calculations limit T/D and M_r to those values that would not allow the cylinders to touch each other, even under the most severe vibration.

In order to establish the credibility of the present numerical method, a thorough comparison of the rigid case is made with previously reported lift and drag calculations and their associated frequencies, and flow visualization results. Two sets of results are selected: one is a numerical investigation reported by Slaouti & Stansby (1992), another is the flow visualization experiment of Zhou *et al.* (2001). The comparisons are made with three different T/D ratios, selected to match those reported by Slaouti & Stansby (1992) and Zhou *et al.* (2001) because the resultant behaviour represents three different flow regimes. Good agreement is obtained between the present and previously reported numerical simulation and experimental visualization. Thus established, the calculations were extended to the vibrating case and the range of T/D selected matches those for the rigid case. The vortex

formation and flow patterns deduced from the calculated results are quite consistent with published data (Williamson 1985). There are no available data to verify the calculations directly. In spite of this, the following conclusions can be drawn from the calculations of the freely vibrating case.

(i) The current numerical technique could reproduce the same phenomena observed in the experiments reported by Williamson (1985), such as the flow patterns at different T/D. This lends further credence to the mechanism of vortex formation reported in the rigid case.
(ii) The proposed moving mesh technique can be used effectively to resolve the flow-induced vibration behaviour in the case of two side-by-side cylinders. This means that the technique could be extended to similar problems with multiple structures.
(iii) At this low Reynolds number, for the rigid cylinder case, vortex shedding is linear; but for the elastic cylinder cases considered, vortex shedding is becoming nonlinear and higher harmonics appear due to fluid–structure interactions. This behaviour is dependent on M_r; the vortex shedding behaviour is still linear for large M_r, but is progressively becoming more nonlinear as M_r decreases.

ACKNOWLEDGEMENT

Support given by The Hong Kong Polytechnic University under Central Research Grant No. G- YC62 and by the Research Grants Council of the Government of the HKSAR under Grant Numbers. PolyU 5159/97E and PolyU 5128/98E are gratefully acknowledged.

REFERENCES

BEARMAN, P. W. 1995 Flow-induced vibration. In *Proceedings of the 6th International Conference on Flow-Induced Vibration*, London, U.K. Rotterdam: A. A. Balkema.

BEARMAN, P. W. & WADCOCK, A. J. 1973 The interaction between a pair of circular cylinders normal to a stream. *Journal of Fluid Mechanics* **61,** 499–511.

BRISTEAU, M. O., GLOWINSKI, R. & PERIAUX, J. 1987 Numerical methods for the Navier–Stokes equations: applications to the simulation of compressible and incompressible viscous flows. *Computer Physics Reports* **6,** 73–187.

CHANG, K. & SONG, C. 1990 Interactive vortex shedding from a pair of circular cylinders in a transverse arrangement. *International Journal for Numerical Methods in Fluids* **11,** 317–329.

JADIC, I., SO, R. M. C. & MIGNOLET, M. P. 1998 Analysis of fluid-structure interactions using a time marching technique. *Journal of Fluids and Structures* **12,** 631–654.

MARPLE, S. L. Jr 1987 *Digital Spectral Analysis with Applications*. Englewood Cliffs, NJ: Prentice-Hall.

MAULL, D. J. 1971 Aerodynamic behaviour of bodies in the wake of other bodies. *Philosophical Transactions of the Royal Society* (*London*) A **269,** 425–437.

MAULL, D. J. & YOUNG, A. D. 1973 Vortex shedding from bluff bodies in a shear flow. *Journal of Fluid Mechanics* **60,** 401–409.

MIGNOLET, M. P. & RED-HORSE, J. R. 1994 ARMAX identification of vibrating structures: model and model order determination. *Proceedings of the 35th Structures, Structural Dynamics, and Materials Conference*, pp. 1628–1637, Hilton Head, South Carolina, U.S.A., April 18–20.

PAIDOUSSIS, M. P. 1998 *Fluid–Structure Interactions—Slender Structures and Axial Flow*. Vol. 1. London: Academic Press.

SLAOUTI, A. & STANSBY, P. K. 1992 Flow around two circular cylinders by the random-vortex method. *Journal of Fluids and Structures* **6,** 641–670.

SO, R. M. C., LIU, Y., CHAN, S. T. & LAM, K. 2001 Numerical studies of a freely vibrating cylinder in a cross flow. *Journal of Fluids and Structures* (in press).

SPIVACK, H. M. 1946 Vortex frequency and flow pattern in the wake of two parallel cylinders at varied spacing normal to an air stream. *Journal of Aeronautical Sciences* **13,** 289–297.

STANSBY, P. K. 1981 A numerical study of vortex shedding from one and two circular cylinders. *Aeronautical Quarterly* **32,** 48–71.

STOKES, N. 1994 Manual of *Fastflo*, Ver. 2. Australia: CSIRO.

SUMNER, D., WONG, S., PRICE, S. J. & PAIDOUSSIS, M. P. 1997 Two and three side-by-side circular cylinders in steady cross-flow. *Proceedings of the* 16*th Canadian Congress of Applied Mechanics*, Quebec City, Canada, Vol. 1, pp. 273–274.

SUMNER, D., WONG, S., PRICE, S. J. & PAIDOUSSIS, M. P. 1999 Fluid behavior of side-by-side circular cylinders in steady cross-flow. *Journal of Fluids and Structures* **13,** 309–338.

TEZDUYAR, T. E., LIOU, J., GANJOO, D. K. & BEHAR, M. 1990 Solution techniques for the vorticity-stream function formulation of two-dimensional unsteady incompressible flows. *International Journal for Numerical Methods in Fluids* **11,** 515–539.

WILLIAMSON, C. H. K. 1985 Evolution of a single wake behind a pair of bluff bodies. *Journal of Fluid Mechanics* **159,** 1–18.

ZDRAVKOVICH, M. M. 1985 Flow-induced oscillations of two interfering circular cylinders. *Journal of Sound and Vibration* **101,** 511–521.

ZDRAVKOVICH, M. M. 1997 *Flow Around Circular Cylinders*, 1st edition. Oxford: Oxford University Press.

ZHOU, C. Y., SO, R. M. C. & LAM, K. 1999 Vortex-induced vibrations of elastic circular cylinders. *Journal of Fluids and Structures* **13,** 165–189.

ZHOU, Y., WANG, Z. J., SO, R. M. C., XU, S. J. & JIN, W. 2001 Free vibrations of two side-by-side cylinders in a cross flow. *Journal of Fluid Mechanics* (accepted).